

Autoencoder-driven Spiral Representation Learning for Gravitational Wave Surrogate Modelling

Paraskevi Nousi^a, Styliani-Christina Fragkouli^a, Nikolaos Passalis^a,
Panagiotis Iosif^c, Theocharis Apostolatos^b, George Pappas^c, Nikolaos
Stergioulas^c, Anastasios Tefas^a

^a*Department of Informatics, Aristotle University of Thessaloniki, Thessaloniki, Greece*

^b*Department of Physics, University of Athens, Athens, Greece*

^c*Department of Physics, Aristotle University of Thessaloniki, Thessaloniki, Greece*

Abstract

Recently, artificial neural networks have been gaining momentum in the field of gravitational wave astronomy, for example in surrogate modelling of computationally expensive waveform models for binary black hole inspiral and merger. Surrogate modelling yields fast and accurate approximations of gravitational waves and neural networks have been used in the final step of interpolating the coefficients of the surrogate model for arbitrary waveforms outside the training sample. We investigate the existence of underlying structures in the empirical interpolation coefficients using autoencoders. We demonstrate that when the coefficient space is compressed to only two dimensions, a spiral structure appears, wherein the spiral angle is linearly related to the mass ratio. Based on this finding, we design a spiral module with learnable parameters, that is used as the first layer in a neural network, which learns to map the input space to the coefficients. The spiral module is evaluated on multiple neural network architectures and consistently achieves better speed-accuracy trade-off than baseline models. A thorough experimental study is conducted and the final result is a surrogate model which can evaluate millions of input parameters in a single forward pass in under 1ms on a desktop GPU, while the mismatch between the corresponding generated waveforms and the ground-truth waveforms is better than the compared baseline methods. We anticipate the existence of analogous underlying structures and corresponding computational gains also in the case of spinning black hole binaries.

Keywords: Gravitational Waves, Autoencoders, Spiral, Surrogate

Modelling

PACS: 0000, 1111

2000 MSC: 0000, 1111

1. Introduction

The first direct detection of gravitational waves (GW) from a binary black hole (BBH) merger in 2015 [1], initiated the era of Gravitational Wave Astronomy. The Advanced LIGO [2] and Advanced Virgo [3] laser interferometric detectors, with arms spanning a few kilometers, can observe stellar-mass and intermediate-mass binary black hole mergers, as well as binary mergers in which one or two components are neutron stars. With consecutive sensitivity improvements, the number of detections has increased from just 3 during the first observing run (O1) [4], to 11 at the end of the second observing run (O2) (comprising the first Gravitational-Wave Transient Catalog (GWTC-1) [5]) and to a total 50 events at the end of the first half of the third observing run (O3a) (comprising GWTC-2 [6]). Furthermore, the international network of GW detectors is expanding with the addition of the KAGRA detector [7] (which already participated in O3) and LIGO-India [8] (expected to join in a few years from today). This development is expected to bolster detection rates and sky-localization accuracies, even more so as the instruments are expected to be upgraded beyond their initial design sensitivity [9].

These discoveries were also enabled by tremendous efforts in modelling of GW sources and data analysis (see e.g. [10, 11, 12, 13, 14, 15, 16, 17, 18, 19, 20, 21, 22, 23, 24, 25, 26, 27, 28, 29, 30, 31]). For non-eccentric BBH mergers, the parameter space λ is seven-dimensional, comprising the mass ratio and the three spin components for each black hole. The numerical-relativity-calibrated effective-one-body (EOB) GW model for binary black hole coalescence SEOBNRv4 [32] only uses three parameters, assuming spins aligned with the orbital angular momentum. In the EOBNRv2 [33] model, the black holes are non-spinning and thus only the mass ratio parameterizes the waveform generation routine.

Waveform generation specifically is of particular importance, as balancing the trade-off between computational speed and waveform faithfulness is a challenging task, with a lot of room for improvements. Towards this end, surrogate modelling [34] can be deployed, wherein the goal is to build a fast surrogate model, which can approximate the waveforms generated from a

computationally slower GW model, within a given tolerance. The surrogate model proposed in [34] for the EOBNRv2 model consists of three steps: First, given a training set of waveforms, a reduced-order-modeling (ROM) basis is obtained (using a greedy algorithm [35]), such that the training set can be reconstructed by multiplying this basis with corresponding coefficients to within a preset error. Second, given the reduced basis, further compression along the time axis is performed, referred to as Empirical Interpolation Method (EIM) [36, 37]. Finally, an interpolation method is used, to obtain fits of the EIM basis coefficients for arbitrary waveforms, which are outside the training set. In practice, such a surrogate model can run significantly faster than required for the generation of the original waveforms.

Further improvements in the computational speed for generating waveforms with a surrogate model were demonstrated in [38], who used artificial neural networks (ANNs) in the third step, in place of traditional interpolation methods. This is an important development, since surrogate-model-parameter fitting with machine-learning (ML) methods has clear computational advantages over traditional methods, especially as the number of physical parameters on which the waveforms depend increases beyond a few (see [39] for a comparison of various interpolation methods for waveform modeling). More generally, ML has emerged as a robust approach for solving a range of problems in GW astronomy, with a rapid increase in use, see e.g. [40] for a recent review.

ANNs pose several advantages over traditional interpolation methods for this task. First, the dimensionality of the input space does not pose as much of a challenge, so long as the training set is sufficiently large and the input space is densely sampled [38]. Second, by leveraging high processing power GPUs, ANNs are able to process hundreds of thousands or even millions of input samples in a single forward pass, depending on the specific architecture. This can lead to extraordinarily large speedups in comparison to traditional interpolation approaches, which are already much faster than evaluating fiducial models [34]. Finally, as universal approximators [41], ANNs are capable of modelling complex relationships, if they have sufficient depth and width.

In this work, we focus on non-spinning EOBNRv2 waveforms and thus work with a 1-dimensional input space, consisting of only the mass ratios between the two BBH components. First, we utilize Autoencoders [42], to investigate the existence of any underlying structure in the coefficients to be fitted. We find that by compressing the coefficient space into only 2 dimensions, *a spiral structure appears, wherein the spiral angle is linearly related*

to the mass ratio. Based on this finding, we design a spiral module with learnable parameters, to be used as the first layer in a neural network, which learns to map the input space to the coefficients. As this structure occurs naturally in a fully unsupervised scenario, we hypothesize, and experimentally show, that the addition of the spiral module leads to faster convergence of the network, as well as to waveform generation that is more faithful to the fiducial waveforms than baseline networks without the module. As a demonstration, we construct a surrogate model for the EOBNRv2 model, which is valid in mass ratios in the interval from 1 to 8 and which can generate up to 1.6 million coefficients in a single forward pass on a desktop GPU, with a worst-case mismatch of 4.33×10^{-7} (several orders of magnitude lower than the mismatches reported in [32]). The existence of the underlying structure, points towards the possible existence of an analogous (higher-dimensional) underlying structure also in the case of spinning BBH mergers, with corresponding anticipated computational improvements.

The remainder of this paper is structured as follows: Section 2 discusses previous related works on surrogate modelling for GW waveforms, as well as autoencoders and representation-driven neural networks. In Section 3, an introduction into surrogate modelling is given first, before moving on to autoencoders and finally to the spiral module. Section 4 is an experimental study into the benefits of the proposed method under various conditions. Finally, Section 5 concludes this study and summarizes its findings.

2. Related Work

A comprehensive framework for surrogate modelling of GW models was given in [34]. Although the method described is model-agnostic, an effective-one-body (EOB) waveform family was used as an example, namely the EOB-NRv2 [33] model, where the input space is 1-dimensional and specifically only the mass ratio is used to generate waveforms. A training set of waveforms is generated first, in a predetermined input space for which the resulting surrogate is valid. Given a sufficiently large training set, the surrogate model should be able to generalize and approximate waveforms outside of the training set. A validation or test set is generated to showcase the surrogate’s ability to generalize.

The proposed framework in [34] consists of three steps. First, given the training set, a linear decomposition problem is solved, resulting to the generation of a reduced basis and corresponding reduced basis coefficients. A

greedy algorithm was proposed for this decomposition which iteratively selects waveforms from the training set to add to the basis. Second, the reduced basis is further reduced with regard to its time dimension. Specifically, time nodes are selected with the Empirical Interpolation Method, which can be used to reconstruct the entirety of the reduced basis. This process results in a modified basis and empirical interpolation coefficients. The final step is to fit the coefficients to the input space, so that the model can be evaluated at arbitrary points in the same interval as the training input space. Since the input space is 1-dimensional, traditional interpolation methods can be used with high accuracy, and it was shown that the resulting surrogate models were significantly faster than the baseline EOBNRv2 generator, while generating waveforms with low mismatches to the ground truth waveforms. Other interpolation methods were compared against each other in [39].

In [43], the waveforms are decomposed into their real and imaginary parts and two surrogate models are created, while the input space for their model is 4-dimensional. ANNs were used to fit the reduced basis coefficients, skipping the empirical interpolation step altogether. Recently, in [38], the waveforms were decomposed into their amplitude and phase signals and two surrogate models are created. The GW model used is the SEOBNRv4 model [41], whose input space is 3-dimensional. Various neural network architectures are investigated for the fitting task and the corresponding mismatches with the ground truth waveforms are reported.

We focus our work on the EOBNRv2 model used in [34], whose input space is 1-dimensional, and do not decompose the complex waveforms. A complex reduced basis is found, upon which the empirical interpolant is built and thus the final empirical interpolation coefficients are complex. Furthermore, we first investigate the underlying relationship between the input space and the coefficients by utilising Autoencoders [42, 44] and by modelling the hidden representation which emerges and has a spiral structure with regard to the mass ratio. We then construct neural network architectures instructed by this finding, by designing a spiral module with learnable parameters. To the best of our knowledge, this is the first work to explore the underlying structure of the empirical interpolation coefficients and apply the knowledge gained to a neural network architecture with a novel module, inspired by the uncovered, physical properties of the coefficients themselves. As demonstrated in Section 4, the added spiral module leads to surrogate waveforms with better mismatches to the ground truth waveforms, while being faster than equivalent architectures, which do not use the module.

3. Background & Proposed Method

3.1. Gravitational wave surrogate models

Let $h(t; \boldsymbol{\lambda}) = h_+(t; \boldsymbol{\lambda}) - ih_\times(t; \boldsymbol{\lambda})$ denote a complex gravitational wave strain [45], as given by a fiducial model, where t denotes time and $\boldsymbol{\lambda}$ denotes the intrinsic parameters. The intrinsic parameters are in general 7-dimensional (mass ratio and two spins with arbitrary orientation) for inspiraling black holes in general relativity, on non-eccentric orbits, but can be simplified under certain restrictions to only include, for example, the mass ratio and two spins aligned with the orbital plane.

The aim of surrogate modelling is to build an approximation of the signal, denoted as $h_s(t; \boldsymbol{\lambda})$, such that $h_s(t; \boldsymbol{\lambda}) \approx h(t; \boldsymbol{\lambda})$ within a threshold of error tolerance. If only the dominant, quadrupole ($l = m = 2$) mode [45] of gravitational-wave emission is considered, then the target is $h_s(t; \boldsymbol{\lambda}) \approx h_{2,2}(t; \boldsymbol{\lambda})$. The first step towards the creation of such a surrogate model is to generate a large set of waveforms and subsequently find a Reduced Basis for this set, using for example a greedy algorithm [34] or Singular Value Decomposition [46]. Following [34], for non-spinning Effective-One-Body (EOB) waveforms of the EOBNRv2 fiducial model [33], the parameter space is one-dimensional and each waveform is parameterized only by the mass ratio q .

Thus, a training set of N waveforms is created¹ $\{h_i(t; q_i)\}_{i=1}^N$ where $q = \frac{m_1}{m_2}$ is the mass ratio of the binary system and limited to a predetermined interval, such as $1 \leq q \leq 2$ for example, for which the surrogate model will be valid. The greedy algorithm chooses a set of $m < N$ waveforms (and their corresponding q values), which constitute the reduced basis $\{e_i\}_{i=1}^m$ after orthonormalization. The basis is built iteratively such that it reconstructs the training set to within a predetermined tolerance as a linear combination of the basis and projection coefficients $\{c_i(q)\}_{i=1}^m$:

$$h(t; q) \approx \sum_{i=1}^m c_i(q) e_i(t). \quad (1)$$

The reconstruction error is measured using the inner product between the reconstructed and the training set waveforms, as per [34], where the inner

¹Waveforms were generated using the PyCBC package [47].

product is given by the complex scalar product:

$$\langle h(\cdot; q_1), h(\cdot; q_2) \rangle = \int_{t_{min}}^{t_{max}} h^*(t; q_1) h(t; q_2) dt, \quad (2)$$

where the star notation denotes complex conjugation. The norm of a waveform is then given by $\|h(\cdot; q)\| = \sqrt{\langle h(\cdot; q), h(\cdot; q) \rangle}$, and waveforms are assumed to be normalized such that $\|h(\cdot; q)\| = 1$ throughout this paper. The overlap integral of a waveform $h(t; q)$ and its corresponding surrogate model prediction $h_s(t; q)$ is given by:

$$\mathcal{O}(h(\cdot; q), h_s(\cdot; q)) = \text{Re} \langle h(\cdot; q), h_s(\cdot; q) \rangle \quad (3)$$

$$= 1 - \frac{1}{2} \|h(\cdot; q) - h_s(\cdot; q)\|^2, \quad (4)$$

and finally, the mismatch between these two waveforms is computed as:

$$\mathcal{M}(h(\cdot; q), h_s(\cdot; q)) = 1 - \mathcal{O}(h(\cdot; q), h_s(\cdot; q)) \quad (5)$$

$$= 1 - \text{Re} \langle h(\cdot; q), h_s(\cdot; q) \rangle. \quad (6)$$

The mismatch between real waveforms and surrogate predictions will be used throughout this paper as a measure of the surrogate's performance.

After the greedy algorithm has converged and the reduced basis has been computed, the second step to surrogate modelling is to recast the problem as one of interpolation in time. Specifically, given a reduced basis $\{e_i(t)\}_{i=1}^m$, the Empirical Interpolation Method (EIM) aims to find a set of points in time, or *empirical nodes*, $\{T_i\}_{i=1}^m$, such that if the values of the fiducial waveforms are known only at these points, the entirety of the fiducial waveform may be recovered with high accuracy for arbitrary q . The result of the EIM method is a new basis that is obtained by imposing on the reduced basis the constraint that the coefficient values are equal to the values of the fiducial waveforms themselves at the empirical time nodes:

$$a_j(q) = h(T_j; q), \quad (7)$$

for all q in the training set. The goal is to fit a model to the coefficients given the corresponding q values present in the training set, such that the surrogate model can approximate any waveform in the range in which it has been trained. Note that using the EOBNRv2 waveform family allows

for the generation of a large training set of N waveforms, leading to dense sampling of empirical interpolation coefficients. Thus, the problem is once again recast as an interpolation problem from input space q to the empirical interpolation coefficients $\mathbf{a}(q) = \{a_j\}_{j=1}^N$. The set of N waveforms have been aligned at the peak of their amplitudes and cropped them to the length of the shortest waveform [38, 34], such that they have a common duration, i.e., time dimension. Finally, the coefficients to be fitted are equal to the values of the training set of waveforms at the empirical time nodes, leading to a dataset \mathcal{D} of pairs of q values and coefficients $\mathbf{a}(q)$:

$$\mathcal{D} = \{(q_i, \mathbf{a}(q_i))\}_{i=1}^N. \quad (8)$$

3.2. Autoencoders

Autoencoders (AE) are a class of unsupervised neural networks which are trained to reconstruct their input, by first mapping it onto an intermediate representation, typically of lower dimension [48], naturally offered for representation learning tasks. In general, an AE consists of an encoding part which maps the input to an intermediate representation, and a decoding part which reconstructs the input and typically has an architecture that is symmetrical to the encoder. The encoder and decoder can consist of multiple layers, each of which is accompanied by learnable parameters, such as the weights and biases of fully connected layers. Let $\mathbf{x} \in \mathbb{R}^D$ denote a D -dimensional input vector. Then an autoencoder can be formally defined by its two parts as:

$$\hat{\mathbf{x}} = f(g(\mathbf{x})), \quad (9)$$

where $g(\cdot)$, $f(\cdot)$ are the encoding and decoding functions respectively, and $\hat{\mathbf{x}} \in \mathbb{R}^D$ is the network's output, which is trained to approximate the input. The encoding and decoding functions can have symmetrical or asymmetrical architectures, and typically consist of multiple layers of, for example, fully connected layers, convolutional layers and even recurrent modules. A useful operation for the decoder in particular is that of transposed convolution, or that of fractionally-strided convolution, used in practice to increase the spatial dimension of feature maps.

Although they are not limited in this scope, typically, AEs are used for dimensionality reduction. In this case, let $\mathbf{y} \in \mathbb{R}^d$, $d < D$, denote the output of the encoder, i.e., $\mathbf{y} = g(\mathbf{x})$, then \mathbf{y} may be regarded as a compressed version of \mathbf{x} . An AE of this form can be trained by minimizing the Mean Square

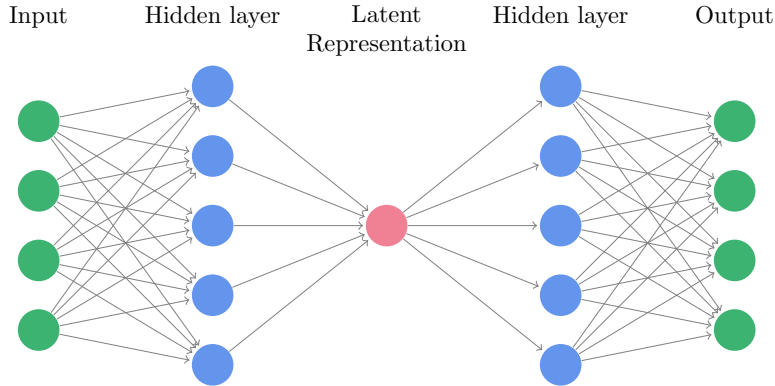


Figure 1: Single hidden layer architecture of a fully connected Autoencoder.

Error (MSE) between the network’s input and output, which corresponds to the reconstruction error:

$$\mathcal{L} = \frac{1}{N} \sum_{i=1}^N \|\hat{\mathbf{x}}_i - \mathbf{x}_i\|_2^2, \quad (10)$$

over all training samples, with respect to the network’s parameters. As data labels are not taken into consideration, an AE trained using the object described here is fully unsupervised. Figure 1 presents a typical architecture for an AE consisting of L fully connected layers. The input and output layer consist of the same number of neurons D . Multiple non-linear layers lead to the intermediate representation. The decoder then tries to reconstruct the input via multiple non-linear layers.

Due to their ability to extract semantically meaningful representations without the use of labels, AEs have been widely studied for a variety of tasks, including clustering [49, 44], classification [42, 50], and image retrieval [51, 52].

Given an EIM coefficient dataset of mass ratio and coefficients pairs $\mathcal{D} = \{(q_i, \mathbf{a}_i)\}_{i=1}^N$, created as described in Section 3.1, training an autoencoder with the coefficients $\mathbf{a}_i = \mathbf{a}(q_i)$ as its input can implicitly aid in uncovering the hidden relationship between each q_i and the corresponding coefficients. The process is unsupervised as the mass ratios are unknown to the autoencoder. Because the pairing of each q_i to the corresponding coefficients \mathbf{a}_i is

known beforehand though, it is possible to use the resulting hidden representation to model the relationship between all q_i and \mathbf{a}_i . As an example, by setting the intermediate representation dimension to $d = 1$, the autoencoder will learn one-dimensional representations y_i for each \mathbf{a}_i , associated with the corresponding q_i . The goal is then to find a mapping from q_i to y_i .

Although this is possible for higher dimensional latent representations as well, in our experiments we set $d = 2$ for simplicity, in which case a spiral pattern emerges, when visualizing the hidden representation as a function of q . This finding is depicted in Figure 5 and discussed in more detail in Section 4.1. On this spiral manifold, the mass ratio q and the spiral angle θ appear to be related in a linear manner, as consecutive angles correspond to consecutive mass ratio values.

3.3. End-to-end Neural Regression with Learnable Spiral

Based on the aforementioned observations, we design and propose the use of a neural spiral module, which first transforms the input q into angles θ :

$$\theta = w \cdot q + b, \quad (11)$$

and subsequently maps θ into a spiral structure of the form:

$$\begin{aligned} s_x &= (\alpha + \beta \cdot \theta) \cdot \cos \theta, \\ s_y &= (\alpha + \beta \cdot \theta) \cdot \sin \theta, \end{aligned} \quad (12)$$

where w, b, α and β are learnable parameters, as the output is differentiable with respect to each of them. Specifically, the partial derivatives are trivially obtained as follows:

$$\begin{aligned} \frac{\partial s_x}{\partial \alpha} &= \cos \theta, \\ \frac{\partial s_x}{\partial \beta} &= \theta \cdot \cos \theta, \end{aligned} \quad (13)$$

(and similarly for s_y). Finally, the errors can be back-propagated to the linear transformation layer, as both s_x and s_y are differentiable with respect to θ :

$$\begin{aligned} \frac{\partial s_x}{\partial \theta} &= \beta \cdot \cos \theta - (\alpha + \beta \cdot \theta) \sin \theta, \\ \frac{\partial s_y}{\partial \theta} &= \beta \cdot \sin \theta + (\alpha + \beta \cdot \theta) \cos \theta. \end{aligned} \quad (14)$$

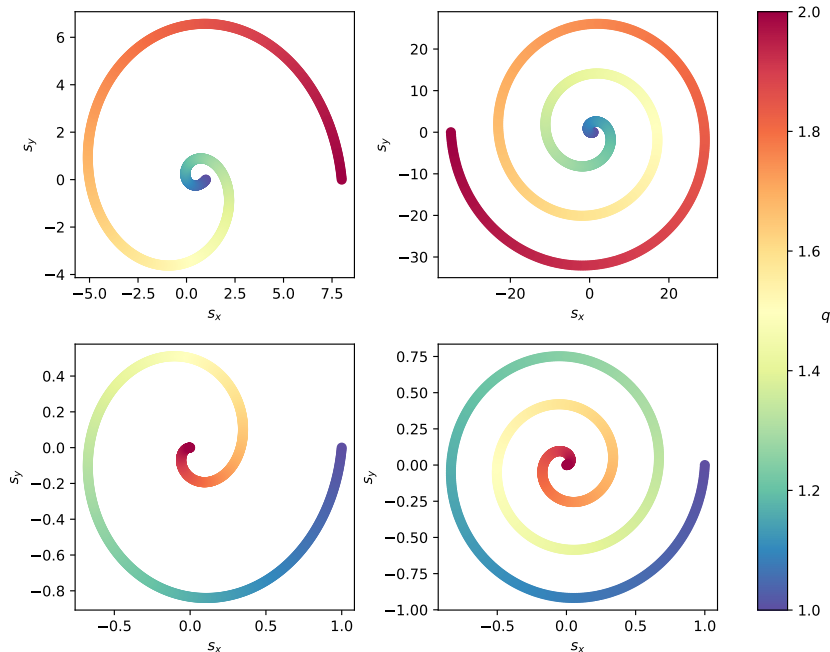


Figure 2: Toy examples of spirals that can be learned with the spiral module in (s_x, s_y) coordinates, given an input q in the range $1 \leq q \leq 2$. The spirals are achieved with the following parameter values: (a) $w = -3\pi$, $b = 3$, $\alpha = 1$, $\beta = 3/\pi$, (b) $w = -6\pi$, $b = 6$, $\alpha = 1$, $\beta = 6/\pi$, (c) $w = -3\pi$, $b = 3$, $\alpha = 1$, $\beta = 1/3\pi$, (d) $w = -6\pi$, $b = 6$, $\alpha = 1$, $\beta = 1/6\pi$.

We hypothesize, and experimentally show in Section 4, that the addition of this module to a typical neural network helps the convergence of the training process to smaller errors. Figure 2 shows some examples of spirals that can be learned with the spiral module, given an input q in the range $1 \leq q \leq 2$. The module can handle various orientations, as well as the degree of coiling. The resulting spiral is then fed to the multiple, subsequent fully-connected layers, each followed by a non-linear activation function, before a final linear layer. An example of this architecture with two hidden layers is shown in Figure 3.

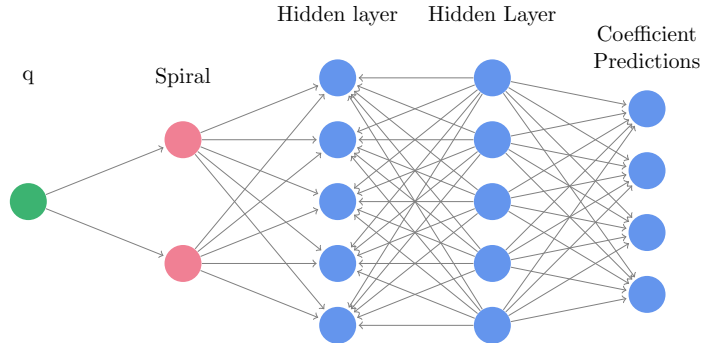


Figure 3: Fully connected neural network with two hidden layers and the proposed spiral module.

4. Experimental Results

4.1. Autoencoder Representation Learning

Following [34], we first consider non-spinning effective-one-body waveforms with mass ratios in the range $1 \leq q \leq 2$. A dataset of $N = 1000$ waveforms is generated and a surrogate model is built as described in Section 3.1, with a tolerance of 10^{-10} , resulting in a reduced basis of size 11. The RomPy package [53] was used to build the reduced basis and perform the empirical interpolation process. The real and imaginary parts of some of these coefficients along with the corresponding q values are shown in Figure 4, where their sinusoidal form relative to q is apparent.

Next, a simple, symmetric encoder-decoder AE architecture is used, with a hidden representation of size $d = 2$, and two hidden fully-connected layers of 128 neurons on either side of the hidden layer. The PReLU non-linearity [54] was used in every layer. We build our models using the PyTorch Deep Learning framework [55]. The empirical interpolation coefficients were used as both the input and output for this network, with the imaginary parts stacked onto the real parts ($D = 2 \cdot 11 = 22$). The AE was trained for 100 epochs with a batch size of 32 and an initial learning rate of 0.001, for which a multiplicative, multi-step schedule was used with a gamma value of 0.9 and a step size of 15. The resulting hidden representation is shown in Figure 5, where the colormap indicates the corresponding q values for each input coefficient. On the spiral manifold, which presents itself in the hidden

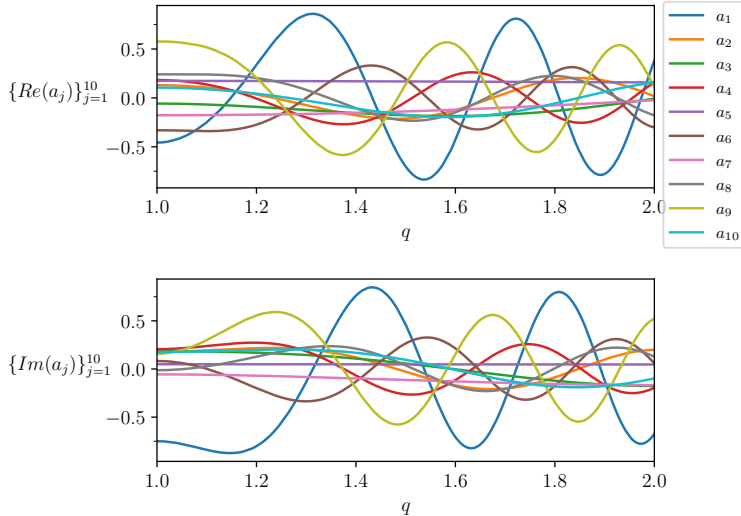


Figure 4: Real (top) and imaginary parts (bottom) of the empirical interpolation coefficients $a_j(q)$ for a surrogate model of EOBNRv2 waveforms that is valid for $1 \leq q \leq 2$.

layer, the relationship between q and the angle θ of the spiral appears to be linear. The final reconstruction MSE is 6.82×10^{-5} .

To gain insight into the spiral formation that appears, we also perform Principal Component Analysis (PCA) [56] on the same dataset and set the number of principal components to 2, i.e. $\mathbf{c}_i \in \mathbb{R}^N$ for $i = 1, 2$. The resulting representation is shown in Figure 6, where a spiral formation also appears. It should be noted that the reconstruction MSE in this case is 3.82×10^{-2} , that is three orders of magnitude larger than that of the AE described previously.

4.2. Learnable Spiral

Based on the above observations, we introduce a spiral module, which transforms the input q into angle θ using Eq. (11) and subsequently into a spiral using Eq. (12). Several neural network architectures with fully-connected layers are evaluated with and without the addition of the spiral module in terms of final waveform mismatch, inference speed as well as their memory requirements, in terms of the maximum batch size that can be processed in a single forward pass on an NVIDIA RTX 2080 Ti GPU. All networks are trained for a total of 2500 epochs, with a batch size of 16 using the Adam

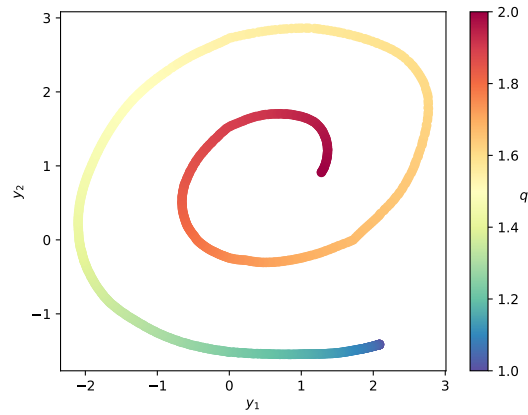


Figure 5: Hidden representation learned by the AE for the empirical interpolation coefficients of a surrogate model of EOBNRv2 waveforms that is valid for $1 \leq q \leq 2$.

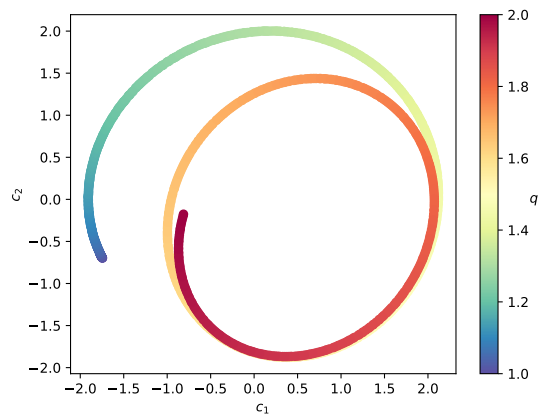


Figure 6: Hidden representation learned by PCA analysis for the empirical interpolation coefficients of a surrogate model of EOBNRv2 waveforms that is valid for $1 \leq q \leq 2$.

optimizer [57] with an initial learning rate of 0.001 which is reduced by 0.95 every 150 epochs.

To obtain a better surrogate model for $1 \leq q \leq 2$, a larger training dataset of $N = 10000$ waveforms is created with equispaced q values, as well as a validation and a test set, each with 2000 waveforms with q values sampled uniformly at random in the same range. We first evaluate a traditional spline fitted on the empirical interpolation coefficients, which achieves a minimum, maximum and average mismatch of 1.05×10^{-12} , 1.26×10^{-8} , and 1.21×10^{-9} respectively. Despite optimizations, the average time needed to produce 10000 waveforms with this method was measured at 0.455s. In contrast, Table 1 summarizes the worst, median and 95th percentile ($p = 95$) mismatch achieved by various neural network architectures, as well as the maximum batch size, which can be executed in a single forward pass. Note that the notation \mathcal{S} in the ‘network’ column denotes the insertion of the spiral module, while each number corresponds to the number of neurons per hidden layer. Note also that because of the somewhat lightweight nature of these neural networks, the overhead when predicting millions of coefficients compared to 10000 coefficients is negligible. Specifically, generating the maximum number of coefficients per architecture takes less than 1ms after optimizations.

The addition of the spiral module consistently improves the mismatch achieved. In the case of only one hidden layer, the baseline network with 128 neurons generates waveforms with very poor mismatch (1.03×10^{-1} median mismatch), whereas with the addition of the spiral module even with as few as only 32 hidden neurons, the median mismatch decreases by about 6 orders of magnitude. The best median and 95th percentile mismatch (9.41×10^{-9} and 3.48×10^{-8}) is achieved by the \mathcal{S} -32-64-128-64 network, which can generate up to 3.4 million coefficients in a single forward pass on the aforementioned GPU.

4.2.1. Extension to larger mass ratios

We finally build a large training dataset of $N = 56000$ waveforms for $1 \leq q \leq 8$, with equispaced q values in this range (corresponding to 8000 values of q per unit interval). A validation and a test set each consisting of 14000 waveforms are created as well, with q values drawn uniformly at random in the interval $1 \leq q \leq 8$ (2000 waveforms per unit interval for each set). Figure 8 shows the real and imaginary parts of the first ten coefficients of the EIM basis, $\{a_j(q)\}_{j=1}^{10}$. In spite of some amplitude modulation, each coefficient has a near sinusoidal dependence with q (except near $q = 1$, where

network	max \mathcal{M}	median \mathcal{M}	$p = 95 \mathcal{M}$	max batch size
128	3.76×10^{-1}	1.03×10^{-1}	3.20×10^{-1}	6.1m
\mathcal{S} -128	1.65×10^{-5}	8.80×10^{-8}	1.32×10^{-6}	6.1m
\mathcal{S} -64	1.54×10^{-5}	2.36×10^{-7}	1.72×10^{-6}	9m
\mathcal{S} -32	1.48×10^{-5}	3.48×10^{-7}	1.65×10^{-6}	11.6m
32-64	6.86×10^{-5}	4.92×10^{-7}	6.13×10^{-6}	7.3m
\mathcal{S} -32-64	1.69×10^{-6}	2.93×10^{-8}	1.35×10^{-7}	7.3m
32-64-128	1.20×10^{-5}	4.79×10^{-8}	6.98×10^{-7}	4.2m
\mathcal{S} -32-64-128	1.05×10^{-7}	3.80×10^{-7}	7.44×10^{-7}	4.2m
32-64-128-64	1.02×10^{-6}	4.47×10^{-8}	1.12×10^{-7}	3.4m
\mathcal{S} -32-64-128-64	1.60×10^{-7}	9.41×10^{-9}	3.48×10^{-8}	3.4m

Table 1: Comparison of various neural network architectures with and without the addition of the spiral module (\mathcal{S}) for $1 \leq q \leq 2$. \mathcal{M} is the mismatch defined in Eq (5). The last column reports the maximum batch size (in millions) that can be processed in a single forward pass on an NVIDIA RTX 2080 Ti GPU .

$dq/da_j = 0$ for all j).

Several neural network architectures were trained and evaluated on this dataset. All networks were trained for a total of 5000 epochs, with a batch size of 32 using the Adam optimizer [57] with an initial learning rate of 0.001, which was reduced by 0.9 every 30 epochs. The results are summarized in Table 2, in terms of the mismatch and of the maximum batch size that can be used during inference, i.e., the maximum number of coefficients that can be generated in a single forward pass. Note that again, these networks are relatively lightweight and the overhead of generating millions of coefficients versus a hundred thousand coefficients is negligible (specifically, a few microseconds). The training and validation loss per epoch for the 32 – 64 – 128 – 64 network and the corresponding architecture with the addition of the spiral is shown in Figure 7. The addition of the spiral leads the network to smaller mean squared errors overall. Note also that no overfitting occurs, which can be attributed to the dense sampling of the input space as well as the high sampling rate used during the generation of the training and validation waveforms. Similar loss curves were observed for the rest of the architectures used as well.

The maximum batch sizes are also shown in Figure 9, as a function of the corresponding 95th percentile ($p = 95$) mismatches, for the baseline model and for the model that includes the spiral module. As with the $1 \leq q \leq 2$ case, the mismatch achieved is consistently better with the addition of the

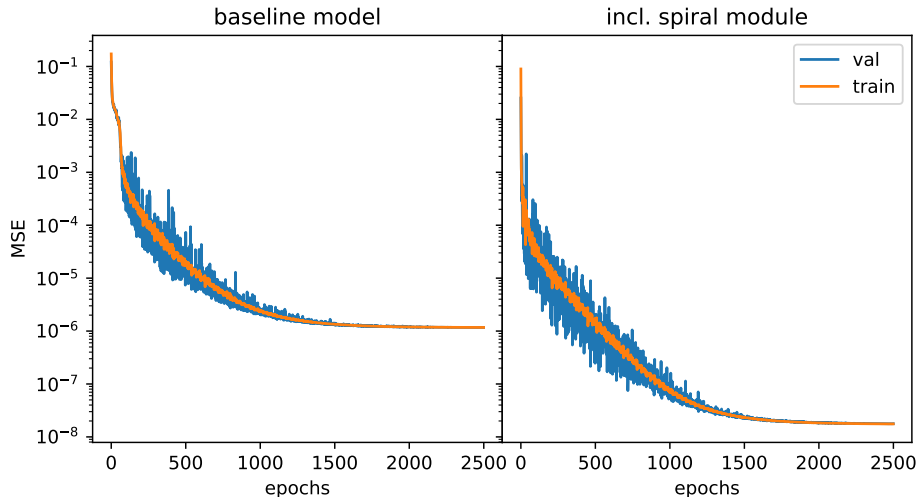


Figure 7: Training and validation loss per epoch for the 32-64-128-64 network and the corresponding architecture with the addition of the spiral.

spiral module. Note the case of 7.3m batch size (32-64 network) in particular, where the inclusion of the spiral module achieves a median mismatch of 1.12×10^{-5} and a worst case mismatch of 4.39×10^{-3} , whereas the respective baseline model achieves a median mismatch of 5.85×10^{-3} and a worst case mismatch of 4.43×10^{-1} , about two orders of magnitude worse. Note also that the most lightweight network converges to an undesirable local minimum, whereas the addition of the spiral leads the network to smaller losses and better mismatches.

5. Conclusions

Recently, artificial neural networks have been gaining momentum in the field of gravitational wave astronomy, and specifically in surrogate modelling of fiducial waveform models. Surrogate modelling yields fast and accurate approximations of gravitational waves and neural networks have been used to interpolate the parameter space to the surrogate coefficients with great success [38]. Our present work focused on non-spinning Effective-One-Body waveforms of the EOBNRv2 model and we investigated the existence of underlying structures in the empirical interpolation coefficients using autoencoders. Subsequently, the spiral structure that was observed in the latent representation uncovered by the AE, inspired the design of a learnable spiral

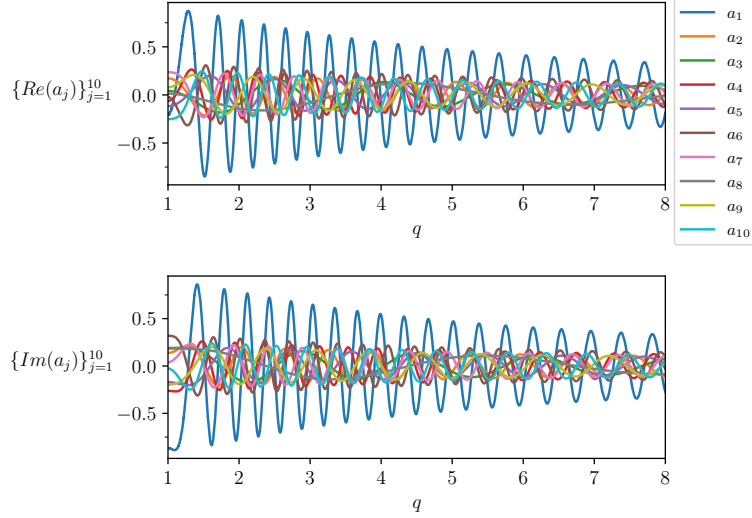


Figure 8: Real (top) and imaginary parts (bottom) of the empirical interpolation coefficients $a_j(q)$ for a surrogate model of EOBNRv2 waveforms that is valid for $1 \leq q \leq 8$.

network	max \mathcal{M}	median \mathcal{M}	$p = 95 \mathcal{M}$	max batch size
16-64	4.36×10^{-1}	1.44×10^{-1}	3.47×10^{-1}	8m
\mathcal{S} -16-64	1.33×10^{-3}	9.14×10^{-5}	2.25×10^{-4}	8m
32-64	4.43×10^{-1}	5.85×10^{-3}	2.84×10^{-1}	7.3m
\mathcal{S} -32-64	4.39×10^{-3}	1.12×10^{-5}	2.56×10^{-5}	7.3m
32-32-64	1.48×10^{-3}	4.97×10^{-5}	1.87×10^{-3}	6.1m
\mathcal{S} -32-32-64	2.99×10^{-5}	9.04×10^{-7}	1.99×10^{-6}	6.1m
32-64-128	9.34×10^{-5}	8.00×10^{-6}	5.83×10^{-5}	4.2m
\mathcal{S} -32-64-128	1.80×10^{-6}	1.66×10^{-7}	3.63×10^{-7}	4.2m
32-64-128-64	7.79×10^{-5}	1.13×10^{-6}	4.62×10^{-6}	3.4m
\mathcal{S} -32-64-128-64	2.55×10^{-6}	4.16×10^{-8}	1.07×10^{-7}	3.4m
64-128-256-128	2.46×10^{-5}	1.50×10^{-7}	2.23×10^{-6}	1.9m
\mathcal{S} -64-128-256-128	5.25×10^{-7}	1.69×10^{-8}	3.93×10^{-8}	1.9m

Table 2: Comparison of various neural network architectures with and without the addition of the spiral module (\mathcal{S}) for $1 \leq q \leq 8$. The various columns are as in Table 1.

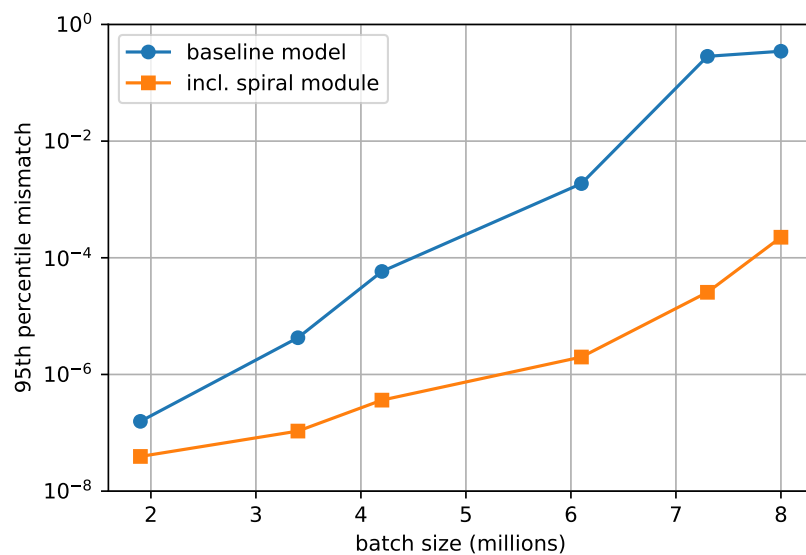


Figure 9: 95th percentile mismatch \mathcal{M} vs. maximum batch size (in millions) for the surrogate EOBNRv2 model in the $1 \leq q \leq 8$ range, where the EIM coefficients were predicted by different baseline neural networks (blue circles) and by corresponding neural networks that included the spiral module (orange boxes), see Table 2. From left to right, the complexity of the neural network decreases, resulting in a larger mismatch, but also in a larger batch size than can be generated on a particular GPU with a single forward pass.

module. The spiral module can be added to any neural network architecture, “*informing*” the network of the physical structure of the coefficients and resulting to waveforms with better mismatches with respect to the ground truth waveforms. Thus, more lightweight architectures can be used in conjunction with the spiral module to generate millions of coefficients in a single batched forward pass, which can be executed in less than 1ms on a desktop GPU.

The existence of the underlying structure in the case of the 1-parameter family of non-spinning waveforms points towards the possible existence of an analogous (higher-dimensional) underlying structure also in the case of spinning BBH mergers, with corresponding anticipated computational improvements. Our initial investigation of spin-aligned waveforms, indeed confirms this anticipation (in preparation).

Acknowledgments

We are grateful to Elena Cuoco, Michael Bejger, Rhys Green, Sebastian Khan and Geraint Pratten for very useful discussions and comments and to the COST network CA17137 “G2Net” for support. The authors gratefully acknowledge the Italian Istituto Nazionale di Fisica Nucleare (INFN), the French Centre National de la Recherche Scientifique (CNRS) and the Netherlands Organization for Scientific Research, for the construction and operation of the Virgo detector and the creation and support of the EGO consortium.

References

- [1] B. Abbott, et al., Observation of Gravitational Waves from a Binary Black Hole Merger, *Physical Review Letters* 116 (6) (2016) 061102. [arXiv:1602.03837](#), [doi:10.1103/PhysRevLett.116.061102](#).
- [2] J. Aasi, et al., Advanced LIGO, *Class. Quant. Grav.* 32 (2015) 074001. [arXiv:1411.4547](#), [doi:10.1088/0264-9381/32/7/074001](#).
- [3] F. Acernese, et al., Advanced Virgo: a second-generation interferometric gravitational wave detector, *Classical and Quantum Gravity* 32 (2) (2014) 024001. [doi:10.1088/0264-9381/32/2/024001](#).
- [4] B. Abbott, et al., Binary Black Hole Mergers in the first Advanced LIGO Observing Run, *Phys. Rev. X* 6 (4) (2016) 041015, [Erratum: *Phys.Rev.X* 8, 039903 (2018)]. [arXiv:1606.04856](#), [doi:10.1103/PhysRevX.6.041015](#).

- [5] B. Abbott, et al., GWTC-1: A Gravitational-Wave Transient Catalog of Compact Binary Mergers Observed by LIGO and Virgo during the First and Second Observing Runs, *Phys. Rev. X* 9 (3) (2019) 031040. [arXiv:1811.12907](#), [doi:10.1103/PhysRevX.9.031040](#).
- [6] R. Abbott, et al., GWTC-2: Compact Binary Coalescences Observed by LIGO and Virgo During the First Half of the Third Observing Run, *Phys. Rev. X* 11 (2021) 021053. [doi:10.1103/PhysRevX.11.021053](#).
- [7] T. Akutsu, et al., KAGRA: 2.5 Generation Interferometric Gravitational Wave Detector, *Nature Astronomy* 3 (1) (2019) 35–40. [doi:10.1038/s41550-018-0658-y](#).
- [8] M. Saleem, J. Rana, V. Gayathri, A. Vijaykumar, S. Goyal, S. Sachdev, J. Suresh, S. Sudhagar, A. Mukherjee, G. Gaur, B. Sathyaprakash, A. Pai, R. X. Adhikari, P. Ajith, S. Bose, The Science Case for LIGO-India, *arXiv e-prints* (2021) [arXiv:2105.01716](#)[arXiv:2105.01716](#).
- [9] B. P. Abbott, et al., Prospects for observing and localizing gravitational-wave transients with Advanced LIGO, Advanced Virgo and KAGRA, *Living Reviews in Relativity* 23 (1) (2020) 3. [doi:10.1007/s41114-020-00026-9](#).
- [10] A. K. Mehta, C. K. Mishra, V. Varma, P. Ajith, Accurate inspiral-merger-ringdown gravitational waveforms for nonspinning black-hole binaries including the effect of subdominant modes, *Physical Review D* 96 (12) (2017) 124010. [arXiv:1708.03501](#), [doi:10.1103/PhysRevD.96.124010](#).
- [11] A. K. Mehta, P. Tiwari, N. K. Johnson-McDaniel, C. K. Mishra, V. Varma, P. Ajith, Including mode mixing in a higher-multipole model for gravitational waveforms from nonspinning black-hole binaries, *Physical Review D* 100 (2) (2019) 024032. [arXiv:1902.02731](#), [doi:10.1103/PhysRevD.100.024032](#).
- [12] S. Khan, F. Ohme, K. Chatziioannou, M. Hannam, Including higher order multipoles in gravitational-wave models for precessing binary black holes, *Physical Review D* 101 (2) (2020) 024056. [arXiv:1911.06050](#), [doi:10.1103/PhysRevD.101.024056](#).

- [13] H. Estellés, A. Ramos-Buades, S. Husa, C. García-Quirós, M. Colleoni, L. Haegel, R. Jaume, IMRPhenomTP: A phenomenological time domain model for dominant quadrupole gravitational wave signal of coalescing binary black holes, arXiv e-prints (2020) arXiv:2004.08302arXiv:2004.08302.
- [14] R. Cotesta, A. Buonanno, A. Bohé, A. Taracchini, I. Hinder, S. Ossokine, Enriching the symphony of gravitational waves from binary black holes by tuning higher harmonics, *Physical Review D* 98 (8) (2018) 084028. arXiv:1803.10701, doi:10.1103/PhysRevD.98.084028.
- [15] A. Nagar, S. Bernuzzi, W. Del Pozzo, G. Riemenschneider, S. Akcay, G. Carullo, P. Fleig, S. Babak, K. W. Tsang, M. Colleoni, F. Messina, G. Pratten, D. Radice, P. Retteno, M. Agathos, E. Fauchon-Jones, M. Hannam, S. Husa, T. Dietrich, P. Cerdá-Duran, J. A. Font, F. Panarale, P. Schmidt, T. Damour, Time-domain effective-one-body gravitational waveforms for coalescing compact binaries with nonprecessing spins, tides, and self-spin effects, *Physical Review D* 98 (10) (2018) 104052. arXiv:1806.01772, doi:10.1103/PhysRevD.98.104052.
- [16] A. Nagar, G. Pratten, G. Riemenschneider, R. Gamba, Multipolar effective one body model for nonspinning black hole binaries, *Physical Review D* 101 (2) (2020) 024041. arXiv:1904.09550, doi:10.1103/PhysRevD.101.024041.
- [17] N. E. M. Rifat, S. E. Field, G. Khanna, V. Varma, Surrogate model for gravitational wave signals from comparable and large-mass-ratio black hole binaries, *Physical Review D* 101 (8) (2020) 081502. arXiv:1910.10473, doi:10.1103/PhysRevD.101.081502.
- [18] V. Varma, S. E. Field, M. A. Scheel, J. Blackman, L. E. Kidder, H. P. Pfeiffer, Surrogate model of hybridized numerical relativity binary black hole waveforms, *Physical Review D* 99 (6) (2019) 064045. arXiv:1812.07865, doi:10.1103/PhysRevD.99.064045.
- [19] S. Khan, K. Chatziioannou, M. Hannam, F. Ohme, Phenomenological model for the gravitational-wave signal from precessing binary black holes with two-spin effects, *Physical Review D* 100 (2) (2019) 024059. arXiv:1809.10113, doi:10.1103/PhysRevD.100.024059.

- [20] V. Varma, S. E. Field, M. A. Scheel, J. Blackman, D. Gerosa, L. C. Stein, L. E. Kidder, H. P. Pfeiffer, Surrogate models for precessing binary black hole simulations with unequal masses, *Physical Review Research* 1 (3) (2019) 033015. [arXiv:1905.09300](#), [doi:10.1103/PhysRevResearch.1.033015](#).
- [21] D. Williams, I. S. Heng, J. Gair, J. A. Clark, B. Khamesra, Precessing numerical relativity waveform surrogate model for binary black holes: A gaussian process regression approach, *Physical Review D* 101 (6) (2020) 063011. [arXiv:1903.09204](#), [doi:10.1103/PhysRevD.101.063011](#).
- [22] S. Ossokine, A. Buonanno, S. Marsat, R. Cotesta, S. Babak, T. Dietrich, R. Haas, I. Hinder, H. P. Pfeiffer, M. Pürrer, C. J. Woodford, M. Boyle, L. E. Kidder, M. A. Scheel, B. Szilágyi, Multipolar effective-one-body waveforms for precessing binary black holes: Construction and validation, *Physical Review D* 102 (4) (2020) 044055. [arXiv:2004.09442](#), [doi:10.1103/PhysRevD.102.044055](#).
- [23] T. Dietrich, S. Khan, R. Dudi, S. J. Kapadia, P. Kumar, A. Nagar, F. Ohme, F. Pannarale, A. Samajdar, S. Bernuzzi, G. Carullo, W. Del Pozzo, M. Haney, C. Markakis, M. Pürrer, G. Riemenschneider, Y. E. Setyawati, K. W. Tsang, C. Van Den Broeck, Matter imprints in waveform models for neutron star binaries: Tidal and self-spin effects, *Physical Review D* 99 (2) (2019) 024029. [arXiv:1804.02235](#), [doi:10.1103/PhysRevD.99.024029](#).
- [24] T. Dietrich, A. Samajdar, S. Khan, N. K. Johnson-McDaniel, R. Dudi, W. Tichy, Improving the NRTidal model for binary neutron star systems, *Physical Review D* 100 (4) (2019) 044003. [arXiv:1905.06011](#), [doi:10.1103/PhysRevD.100.044003](#).
- [25] G. Pratten, S. Husa, C. García-Quirós, M. Colleoni, A. Ramos-Buades, H. Estellés, R. Jaume, Setting the cornerstone for a family of models for gravitational waves from compact binaries: The dominant harmonic for nonprecessing quasicircular black holes, *Physical Review D* 102 (6) (2020) 064001. [arXiv:2001.11412](#), [doi:10.1103/PhysRevD.102.064001](#).
- [26] L. London, S. Khan, E. Fauchon-Jones, C. García, M. Hannam, S. Husa, X. Jiménez-Forteza, C. Kalaghatgi, F. Ohme, F. Pannarale, First higher-

- multipole model of gravitational waves from spinning and coalescing black-hole binaries, *Physical Review Letters* 120 (16) (2018) 161102. [arXiv:1708.00404](#), [doi:10.1103/PhysRevLett.120.161102](#).
- [27] A. Nagar, G. Riemenschneider, G. Pratten, P. Rettengo, F. Messina, Multipolar effective one body waveform model for spin-aligned black hole binaries, *Physical Review D* 102 (2) (2020) 024077. [arXiv:2001.09082](#), [doi:10.1103/PhysRevD.102.024077](#).
- [28] G. Pratten, C. García-Quirós, M. Colleoni, A. Ramos-Buades, H. Estellés, M. Mateu-Lucena, R. Jaume, M. Haney, D. Keitel, J. E. Thompson, S. Husa, Computationally efficient models for the dominant and subdominant harmonic modes of precessing binary black holes, *Physical Review D* 103 (2021) 104056. [doi:10.1103/PhysRevD.103.104056](#).
- [29] C. García-Quirós, M. Colleoni, S. Husa, H. Estellés, G. Pratten, A. Ramos-Buades, M. Mateu-Lucena, R. Jaume, Multimode frequency-domain model for the gravitational wave signal from nonprecessing black-hole binaries, *Physical Review D* 102 (6) (2020) 064002. [arXiv:2001.10914](#), [doi:10.1103/PhysRevD.102.064002](#).
- [30] R. Abbott, et al., GW190412: Observation of a Binary-Black-Hole Coalescence with Asymmetric Masses, *Phys. Rev. D* 102 (4) (2020) 043015. [arXiv:2004.08342](#), [doi:10.1103/PhysRevD.102.043015](#).
- [31] R. Abbott, et al., GW190814: Gravitational Waves from the Coalescence of a 23 Solar Mass Black Hole with a 2.6 Solar Mass Compact Object, *Astrophys. J.* 896 (2) (2020) L44. [arXiv:2006.12611](#), [doi:10.3847/2041-8213/ab960f](#).
- [32] A. Bohé, L. Shao, A. Taracchini, A. Buonanno, S. Babak, I. W. Harry, I. Hinder, S. Ossokine, M. Pürrer, V. Raymond, et al., Improved effective-one-body model of spinning, nonprecessing binary black holes for the era of gravitational-wave astrophysics with advanced detectors, *Physical Review D* 95 (4) (2017) 044028.
- [33] Y. Pan, A. Buonanno, M. Boyle, L. T. Buchman, L. E. Kidder, H. P. Pfeiffer, M. A. Scheel, Inspiral-merger-ringdown multipolar waveforms of nonspinning black-hole binaries using the effective-one-body formalism, *Physical Review D* 84 (12) (2011) 124052.

- [34] S. E. Field, C. R. Galley, J. S. Hesthaven, J. Kaye, M. Tiglio, Fast prediction and evaluation of gravitational waveforms using surrogate models, *Physical Review X* 4 (3) (2014) 031006.
- [35] T. H. Cormen, C. E. Leiserson, R. L. Rivest, C. Stein, *Introduction to Algorithms*, 3rd Edition, MIT Press, 2009.
- [36] M. Barrault, Y. Maday, N. C. Nguyen, A. T. Patera, An ‘empirical interpolation’ method: application to efficient reduced-basis discretization of partial differential equations, *Comptes Rendus Mathematique* 339 (9) (2004) 667–672.
- [37] Y. Maday, N. C. Nguyen, A. T. Patera, S. H. Pau, A general multi-purpose interpolation procedure: the magic points, *Communications on Pure and Applied Analysis* 8 (1) (2009) 383–404.
- [38] S. Khan, R. Green, Gravitational-wave surrogate models powered by artificial neural networks, *Physical Review D* 103 (6) (2021) 064015.
- [39] Y. Setyawati, M. Pürrer, F. Ohme, Regression methods in waveform modeling: a comparative study, *Classical and Quantum Gravity* 37 (7) (2020) 075012.
- [40] E. Cuoco, J. Powell, M. Cavaglià, K. Ackley, M. Bejger, C. Chatterjee, M. Coughlin, S. Coughlin, P. Easter, R. Essick, H. Gabbard, T. Gebhard, S. Ghosh, L. Haegel, A. Iess, D. Keitel, Z. Márka, S. Márka, F. Morawski, T. Nguyen, R. Ormiston, M. Pürrer, M. Razzano, K. Staats, G. Vajente, D. Williams, Enhancing gravitational-wave science with machine learning, *Machine Learning: Science and Technology* 2 (1) (2020) 011002. doi:10.1088/2632-2153/abb93a.
- [41] S. Sonoda, N. Murata, Neural network with unbounded activation functions is universal approximator, *Applied and Computational Harmonic Analysis* 43 (2) (2017) 233–268.
- [42] P. Nousi, A. Tefas, Deep learning algorithms for discriminant autoencoding, *Neurocomputing* 266 (2017) 325–335.
- [43] A. J. Chua, C. R. Galley, M. Vallisneri, Reduced-order modeling with artificial neurons for gravitational-wave inference, *Physical Review Letters* 122 (21) (2019) 211101.

- [44] P. Nousi, A. Tefas, Self-supervised autoencoders for clustering and classification, *Evolving Systems* (2018) 1–14.
- [45] M. Maggiore, *Gravitational Waves Volume 1: Theory and Experiments*, Oxford University Press, 2008. doi:10.1093/acprof:oso/9780198570745.001.0001.
- [46] J. Blackman, S. E. Field, M. A. Scheel, C. R. Galley, D. A. Hemberger, P. Schmidt, R. Smith, A surrogate model of gravitational waveforms from numerical relativity simulations of precessing binary black hole mergers, *Physical Review D* 95 (10) (2017) 104023.
- [47] A. Nitz, I. Harry, D. Brown, C. M. Biwer, J. Willis, T. D. Canton, C. Capano, T. Dent, L. Pekowsky, A. R. Williamson, G. S. C. Davies, S. De, M. Cabero, B. Machenschalk, P. Kumar, D. Macleod, S. Reyes, dfinstad, F. Pannarale, T. Massinger, S. Kumar, M. Tápai, L. Singer, S. Khan, S. Fairhurst, A. Nielsen, S. Singh, shasvath, B. U. V. Gadre, I. Dorrington, gwastro/pycbc: Pycbc release 1.18.1 (May 2021). doi: 10.5281/zenodo.4849433.
URL <https://doi.org/10.5281/zenodo.4849433>
- [48] P. Vincent, H. Larochelle, Y. Bengio, P.-A. Manzagol, Extracting and composing robust features with denoising autoencoders, in: *Proceedings of the 25th international conference on Machine learning*, 2008, pp. 1096–1103.
- [49] J. Xie, R. Girshick, A. Farhadi, Unsupervised deep embedding for clustering analysis, in: *International conference on machine learning*, 2016, pp. 478–487.
- [50] P. Nousi, A. Tefas, Discriminatively trained autoencoders for fast and accurate face recognition, in: *International Conference on Engineering Applications of Neural Networks*, Springer, 2017, pp. 205–215.
- [51] P. Wu, S. C. Hoi, H. Xia, P. Zhao, D. Wang, C. Miao, Online multi-modal deep similarity learning with application to image retrieval, in: *Proceedings of the 21st ACM international conference on Multimedia*, 2013, pp. 153–162.

- [52] M. A. Carreira-Perpinán, R. Raziperchikolaei, Hashing with binary autoencoders, in: Proceedings of the IEEE conference on computer vision and pattern recognition, 2015, pp. 557–566.
- [53] C. R. Galley, RomPy package, <https://bitbucket.org/chadgalley/rompy/> (2020).
- [54] K. He, X. Zhang, S. Ren, J. Sun, Delving deep into rectifiers: Surpassing human-level performance on imagenet classification, in: Proceedings of the IEEE international conference on computer vision, 2015, pp. 1026–1034.
- [55] A. Paszke, S. Gross, S. Chintala, G. Chanan, E. Yang, Z. DeVito, Z. Lin, A. Desmaison, L. Antiga, A. Lerer, Automatic differentiation in pytorch, in: NIPS-W, 2017.
- [56] H. Abdi, L. J. Williams, Principal component analysis, Wiley interdisciplinary reviews: computational statistics 2 (4) (2010) 433–459.
- [57] D. P. Kingma, J. Ba, Adam: A method for stochastic optimization, arXiv preprint arXiv:1412.6980 (2014).